A&A manuscript no.
(will be inserted by hand later)

Your thesaurus codes are:
06

ASTRONOMY
AND
ASTROPHYSICS
October 4, 2000

The European Photon Imaging Camera on XMM-Newton: The MOS Cameras

M. J. L. Turner[1], A. Abbey[1], M. Arnaud[2], M. Balasini[13], M. Barbera[10], E. Belsole[2], P. J. Bennie[1], J. P. Bernard[12], G. F. Bignami[7], M. Boer[3], U. Briel[4], I. Butler[5], C. Cara[2], C. Chabaud[3], A. Collura[10], M. Conte[7], A. Cros[3], M. Denby[1], P. Dhez[6], G. Di Coco[11], J. Dowson[1], P. Ferrando[2], S. Ghizzardi[7], F. Gianotti[11], C. V. Goodall[5], L. Gretton[1], R. G. Griffiths[1], O. Hainaut[12], J. F. Hochedez[12], A. D. Holland[1], E. Jourdain[12], E. Kendziorra[8], A. Lagostina[7], R. Laine[9], N. La Palombara[7], M. Lortholary[2], D. Lumb[14], P. Marty[12], S. Molendi[7], C. Pigot[2], E. Poindron[2], K. A. Pounds[1], J. N. Reeves[1], C. Reppin[4], R. Rothenflug[2], P. Salvetat[12], J. L. Sauvageot[2], D. Schmitt[2], S. Sembay[1], A. D. T. Short[1], J. Spragg[1], J. Stephen[11], L. Strüder[4], A. Tiengo[7], M. Trifoglio[11], J. Trümper[4], S. Vercellone[7], L. Vigroux[2], G. Villa[7], M. J. Ward[1], S. Whitehead[1], and E. Zonca[2]

[1] Dept. of Physics & Astronomy, Leicester University, LE1 7RH, UK.
[2] CEA/DSM/DAPNIA Service d'Astrophysique, CEA/Saclay, 91191 Gif-sur-Yvette Cedex, France.
[3] Centre d'Etude Spatiale des Rayonnements, 9 avenue du colonel Roche, BP 4346, 31028 Toulouse Cedex 4, France.
[4] MPE D-85740 Garching, 8046, Germany.
[5] School of Physics and Astronomy, University of Birmingham, B15 2TT, UK.
[6] Laboratoire pour l'Utilisation du Rayonnement Electromagnetique, Bat 209 D, Universite Paris Sud, 91405 Orsay, France.
[7] IFC Milan, 20133 Milano, Italy.
[8] IAAP Tuebingen, D-72076, Germany
[9] PX Estec, Postbus 299, 2200 AG Noordwijk, Holland.
[10] Osservatorio Astronomico di Palermo, Palermo, 90134, Italy.
[11] ITESRE, 41010 Bologna,Italy.
[12] Institut d'Astrophysique Spatiale, Bat 121, Université Paris Sud, 91405 Orsay, France
[13] Laben S.p.A, S.S. Padana Superiore, 290, 20090 Vimodrone, Milano, Italy
[14] Space Science Department, ESTEC, 2200 AG Noordwijk, Holland

Received; accepted

Abstract. The EPIC focal plane imaging spectrometers on XMM-Newton use CCDs to record the images and spectra of celestial X-ray sources focused by the three X-ray mirrors. There is one camera at the focus of each mirror; two of the cameras contain seven MOS CCDs, while the third uses twelve PN CCDs, defining a circular field of view of $30'$ diameter in each case. The CCDs were specially developed for EPIC, and combine high quality imaging with spectral resolution close to the Fano limit. A filter wheel carrying three kinds of X-ray transparent light blocking filter, a fully closed, and a fully open position, is fitted to each EPIC instrument. The CCDs are cooled passively and are under full closed loop thermal control. A radio-active source is fitted for internal calibration. Images are processed on-board to compress the data by removing cosmic ray tracks, and generating X-ray event files; a variety of different instrument modes are available to increase the dynamic range of the instrument and to enable fast timing. The instruments were calibrated using laboratory X-ray beams, and synchrotron generated monochromatic X-ray beams before launch; in-orbit calibration makes use of a variety of celestial X-ray targets. The current calibration is better than 10% over the entire energy range of 0.2 to 10 keV. All three instruments survived launch and are performing nominally in orbit. In particular full field-of-view coverage is available, all electronic modes work, and the energy resolution is close to pre-launch values. Radiation damage is well within pre-launch predictions and does not yet impact on the energy resolution. The scientific results from EPIC amply fulfil pre-launch expectations.

Key words: Instrumentation: detectors - X-rays: general

1. Introduction

The EPIC instrument on XMM-Newton (Jansen et al., 2001) provides focal plane imaging and spectrometry for the three X-ray telescopes. Each telescope has an objective comprising a nested, 58 shell, Wolter 1 X-ray mirror (Aschenbach et al., 2001), of focal length 7.5 metres, and geometric effective area 1500 cm^2; there is one EPIC at the focus of each telescope. Two of the telescopes are fitted with the X-ray gratings of the Reflection Grating Spectrometer (Brinkman et al., 2001). The gratings divert 50% of the flux out of the EPIC beams; with allowance for structural obscuration, 40% of the original flux reaches two of the EPIC cameras; these contain MOS CCDs (Short et al., 1998) and are referred to as the MOS cameras. The

---

Send offprint requests to: M. J. L. Turner

Fig. 1. The long conical radiators of the MOS enable the radiating surface to reach the plane of the spacecraft thermal shield to avoid parasitic heat-loads.

third telescope has an unobstructed beam; the EPIC instrument at the focus of this telescope uses PN CCDs (Strüder et al., 2001) and is referred to as the PN camera. All three cameras have an identical forward section that contains a filter wheel, door, calibration source, radiation shielding, the interface to the spacecraft focal plane bulkhead, and the internal bulkhead that forms part of the camera vacuum enclosure. The rear part of each camera that contains the CCDs and the cooling system is different in construction for the MOS and PN cameras. These differences arise both because of the different CCDs, and because of the different locations of the three cameras on the spacecraft focal plane bulkhead. The two MOS cameras are located symmetrically, near the spacecraft sun-shield, and consequently have long radiators, while the PN is close to the anti-sun, and has a short radiator. The MOS camera is shown in figure 1. The electronic boxes for the three cameras are located on the spacecraft focal plane bulkhead, adjacent to the cameras. EPIC also includes the EPIC Radiation Monitor System, to record the ambient proton and electron flux. The detectors of the ERMS (Boër et al., 1996) are located on the outside of the spacecraft, within the ambient radiation. It provides warning of a radiation flux increase to provide for automatic shut down of the instrument. This paper describes the common items and the MOS cameras, while an accompanying paper, by Strüder et al. (2001) describes the PN camera.

2. The EPIC Camera Configuration

Each EPIC camera has three sections: the stand-off structure that contains the filter wheel, door, calibration source, interface to the spacecraft, the radiation shield and the internal vacuum bulkhead; the cryostat section that contains the CCDs and electronic interfaces, and the radiator that provides the cooling for the CCDs. The stand-off-structure is identical for all three cameras, and is described here; the remaining sections are different for PN (Strüder et al., 2001) and MOS (see below).

2.1. The Stand-off Structure

The structure, shown in figure 2, is a nickel-plated cylindrical aluminium machining, with a vacuum bulkhead containing feed-throughs for the filter wheel drive and electronic connections. The bulkhead forms the forward part of the vacuum enclosure when the stand-off structure is sealed to the cryostat via an O-ring and a bolted flange. The purpose of the vacuum is to protect the CCDs from contamination before launch, and to protect the filters from acoustic damage during launch. The filter wheel with its gears and motor is located on the vacuum side of the bulkhead (figure 2, bottom panel). It is driven by a gear and pinion, and has six locations for filters, and six small apertures through which the calibration source can shine onto the CCDs. The source itself is mounted in the bulkhead, on the vacuum side. The aperture in the bulkhead through which the X-rays reach the CCDs is closed before and during launch by the door. The door is mounted on a spring-loaded arm, and is clamped by an integral set of double stainless steel bellows that, when pressurised, press a plate on to an O-ring mounted in the bulkhead. When the nitrogen pressure of 4 bar is released, the bellows retract, and the door swings out of the aperture, under action of the spring. The CCDs are protected from damaging proton irradiation by at least 3 cm of aluminium shielding in all directions, except the field of view; part of this shielding is incorporated in the cryostats, and part in the stand-off structure. The latter is in two parts: an internally mounted shield between the bulkhead and the CCDs, this has a narrow gap beneath the bulkhead within which the filters are positioned; and a separate shield, mounted on the spacecraft focal plane bulkhead that completes the forward shielding by projecting up the telescope tube towards the mirrors. These shields are internally blackened to reduce optical stray-light.

2.2. The MOS Cryostat

The cryostat is a conical nickel-plated aluminium structure that interfaces to the stand-off structure. The cold-finger is supported by aluminium and GFRP components forming a doubly insulated structure with a secondary thermal shield, thermally linked to the outer radiator. The CCDs are mounted on the end of the cold finger, and the rear 3 cm shielding is integral with the CCD mounting plate. The CCDs themselves are mounted on individual packages: the CCD is first bonded to a silicon substrate; this is bonded to an invar plate that is in turn bolted and bonded to an aluminium locating block. Each block slides in a channel in the mounting plate; the CCDs are located accurately by this channel (figure 4). The heaters for thermal control are incorporated in the mounting plate, which

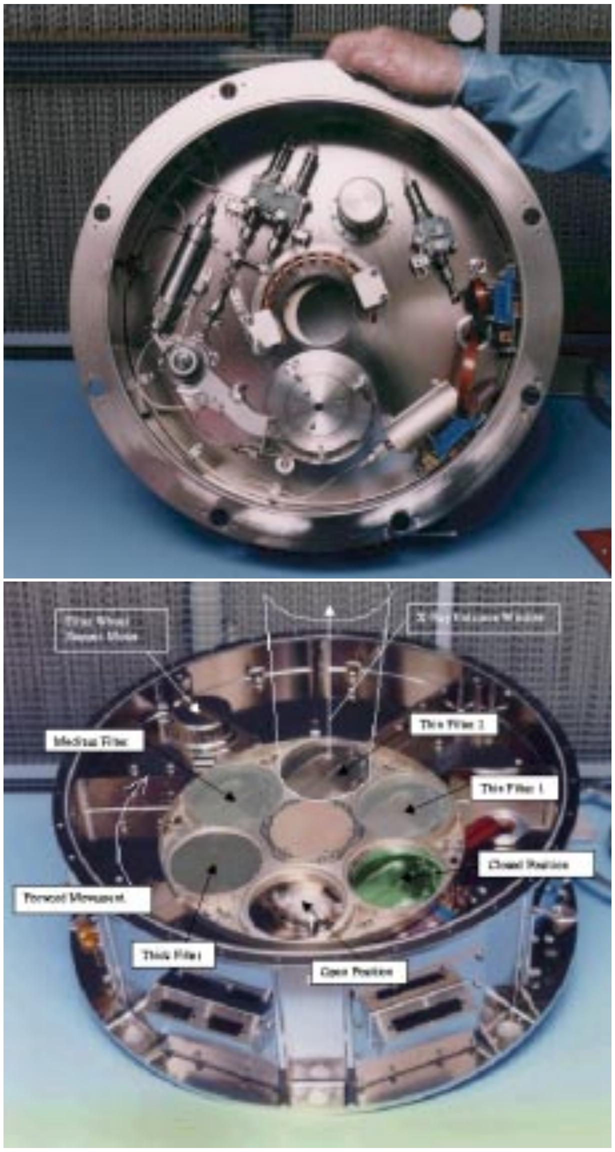

Fig. 2. The EPIC Stand-off Structure. The aluminium machining is nickel plated to reduce vacuum out-gassing. It houses the filter wheel, calibration source and door; the bulkhead is part of the vacuum enclosure. It is located on the spacecraft bulkhead using drilled bushes to bring the optical centre of the camera to the optical axis of the mirror.

is at the operational temperature of the CCDs (∼170 K). Electrical connections to the CCDs and to the heaters are made with thin flexible printed circuits, to provide a thermal break. The preamplifiers and other electrical components are mounted on an external conventional multi-layer PCB. The PCB also acts as the vacuum feed-through to bring signals and power into the cryostat. It is trapped between two O-rings to make a vacuum seal; the electrical signals travel on internal layers in the board. The cryostat is closed at the rear with two 50 micron stainless steel foils that link the outer and inner thermal shields to the cold finger; they provide a vacuum and EMC tight connection with minimal thermal conductivity.

2.3. The MOS Radiators

The MOS cryostat is cooled passively (Butler and Goodall, 2000) by the system of three nested conical radiators. This shape is necessitated by the distance between the CCD focal plane and the top of the spacecraft sun-shield. To avoid parasitic thermal radiation load from the spacecraft all radiating surfaces need to be in the plane of the shielded zone. The radiator cones are truncated at an angle to match the slope of the shielded zone and have flanges formed on them. The radiators provide successive thermal shielding for the inner radiator which is attached to the CCD via the cold finger. This inner radiator is mechanically supported by the cold finger and has no contact with the other radiators. The outer radiator carries the exterior multilayer insulation on its outer face and the secondary radiator on its inner face. The latter radiator is connected to the thermal shroud surrounding the CCD and cold finger via a flexible thermal coupling. Doubly aluminised Mylar foils independently suspended between successive radiator cones provide additional shielding thus enhancing performance and robustness against deterioration in space of the thermal finish of surfaces. The radiators are made of spun aluminium of 0.6 mm thickness. The inner radiator is painted with white epoxy paint to give maximum emissivity, coupled with low absorptivity for Earth albedo during perigee. The cooling system provides a minimum temperature at the CCD of 140 K. The radiators are supported from a strong-ring on the cryostat by GFRP struts. The whole system including the cold finger is very stiff so as to reduce vibration loads on the attached CCDs.

3. The Electronics

The electronic block diagram is shown in figure 3. There are four boxes for each MOS camera (Villa et al., 1996). The preamplifiers are mounted on the cryostat PCB, integral with the camera. These interface via the harness to the analogue electronics box EMAE. This conditions the signals and contains the CCD clock sequencers. The system is partially redundant with one set of eight channels reading out the seven CCDs in a camera. There are two readout nodes on each CCD. The outer six CCDs are normally read from one node, and the central CCD can be read from one node, or for faster response by two in parallel. The second of each pair of processing chains is connected to the alternate nodes of the outer CCDs; multiplexers allow crossover in the case of failure. The EMAE also contains the clocking sequencers that generate the trains of pulses to transfer the charge released by the X-rays to the readout node. The control and recognition unit EMCR (Pigot et al., 2000; Ferrando et al., 1999) has the main function of converting the image read out from each CCD into an X-ray photon event list. This uses fast logic (an ASIC) to subtract offsets so that the energy scale starts at zero; it identifies geometric patterns of pixels using a look up table, programmable from the ground, to distinguish between those produced by X-rays and those produced by cosmic rays. It also adds up the charge over the pattern in each event to enable the X-ray energy to be determined accurately. The output is an event list with several

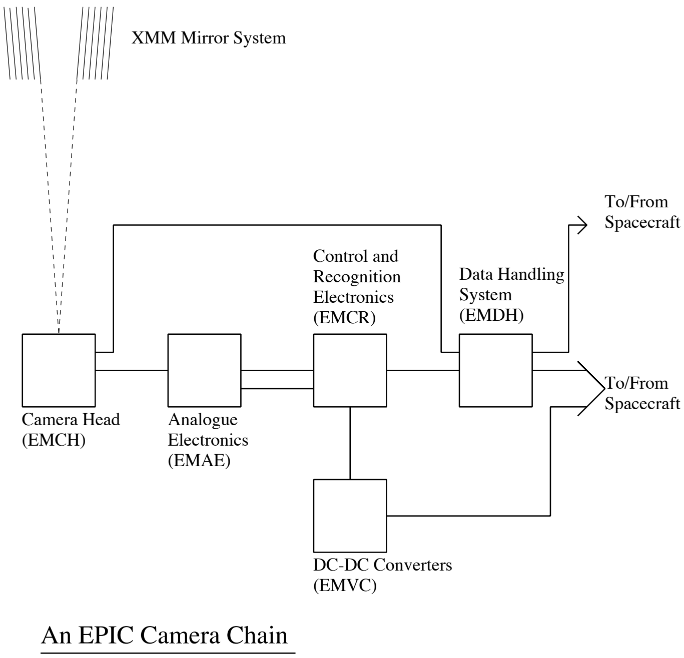

Fig. 3. The EPIC MOS electronics block diagram

different energy parameters attached, together with the pattern shape. Converting the image into an event list results in significant data compression, because of the sparse nature of the X-ray image. The pattern recognition enables cosmic rays to be rejected on-board. The other function of the EMCR is to store and transmit CCD clock sequences for the different modes to the CCD clock sequencers in the EMAE; it also provides the control signals to the filter wheel and timestamps CCD frames. Power conditioning and distribution is provided by the voltage controller, EMVC. This receives raw spacecraft power from the bus and provides the necessary voltages and currents to all the other boxes. It is fully redundant. The data handling and interface to the spacecraft data system and telemetry is provided by the EMDH (Villa et al., 1996). This receives data from the EMCR and conditions it for the telemetry. It receives, distributes, and executes commands; it also contains the on-board software that controls the instrument modes. The EMDH controls all instrument safety aspects and is the interface to the spacecraft for software upload, command and data handling.

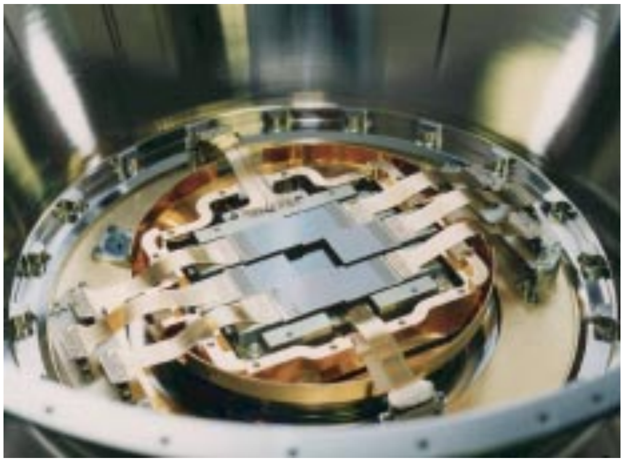

Fig. 4. The CCDs with their flexible PCB links shown mounted in the cryostat

4. The CCDs

There are seven EEV type 22 CCDs in the focal plane of each MOS camera (Short et al., 1998), arranged as shown in figure 4. The central CCD is at the focal point on the optical axis of the telescope while the outer six are stepped towards the mirror by 4.5 mm to follow approximately the focal plane curvature, and improve the focus for off-axis sources. The CCDs are buttable with a dead region about 350 microns wide on three sides; to minimise the dead space, adjacent CCDs are stepped by about 1mm to overlap by 350 microns. The EEV CCD22 is a three-phase frame transfer device on high resistivity epitaxial silicon with an open-electrode structure; it has a useful quantum efficiency in the energy range 0.2 to 10 keV. The imaging area is $\sim$ 2.5 x 2.5 cm, so that a mosaic of seven covers the focal plane 62 mm in diameter, equivalent to $28'.4$. The imaging section has 600 x 600, 40 micron square, pixels; one pixel covers 1.1 x 1.1 arc seconds on the field of view; 15 pixels cover the mirror PSF half energy width of $15''$. The store has 600 x 602, 39 x 12 micron, pixels. The readout register is split into two sections, each of 300+5 elements, ending in a readout node. The full CCD image can be read out using either node, or read out using both nodes simultaneously, to halve the readout time. The low energy response of the conventional front illuminated CCD is poor below $\sim$700 eV because of absorption in the electrode structure. For EPIC, one of the three electrodes has been enlarged to occupy a greater fraction of each pixel, and holes have been etched through this enlarged electrode to the gate oxide. This gives an 'open' fraction of the total pixel area of 40%; this region has a high transmission for very soft X-rays that would otherwise be absorbed in the electrodes. In the etched areas, the surface potential is pinned to the substrate potential by means of a 'pinning implant'. High energy efficiency is defined by the resistivity of the epitaxial silicon (around 4000 Ohm-cm). The epitaxial layer is 80 microns thick (p-type). The actual mean depletion of the flight CCDs is between 35 and 40 microns: the open phase region of each pixel is not fully depleted. The two MOS cameras are arranged on the spacecraft focal plane bulkhead so that the CCDs are orthogonal. This means that the 350 micron gaps between the outer CCDs in one camera are covered by their opposite numbers in the other camera. The gaps around the central CCD in either camera exactly overlap: so a source falling in this gap in MOS1 will also be in the gap in MOS2. The PN CCDs are arranged at 45 degrees to the two MOS cameras so the field of view is fully covered among the three EPIC cameras.

5. The EPIC MOS Readout Modes

The basic readout speed of the MOS CCDs is 2.6 seconds; this is the same as the integration time, and is available continuously on all seven CCDs in each camera. The only reason to change this is if the source is bright: pile up may be a problem; or there may be an opportunity for fast timing observations. The modes comprise 'large and small window mode', 'refreshed frame store mode' (see Willingale et al., 2001) and 'timing mode'. Window mode can be applied to the central CCD and independently to the peripheral CCDs in pairs (not used at present). A window is defined on the CCD (windows need not be central on the CCD) and rows and pixels outside this window are discarded on readout. Since most of the readout time is taken up by measuring the pixel charge accurately, this results in a much faster readout and integration. Two window sizes are currently implemented: Large window 300 × 300 pixels centred - 0.9 s integration time. Small window 100 × 100 centred - 0.3 s integration time. In full frame mode, an electronic chopper can be implemented - "Refreshed frame store mode" which discards most of the X-rays collected during readout and integrates for 0.2 seconds. The overall cycle time is 2.9 s leading to a duty cycle of 1:14.7. Selection of the window size is a compromise between readout speed and field of view coverage: source extent, and the PSF wings may require a larger window. The window is only applied to the central CCD, the peripheral CCDs remain fully operational and the only area lost is the region outside the window on the central CCD. For timing mode - also known as "Fast mode" - 100 rows in a central window 100 pixels wide are compressed into one dimension, parallel to the CCD readout register to give fast time slices of the incoming X-ray flux. The CCD output node is only reset once per row to give a constant timebase (unlike the standard "reset-on-demand"), and the EDU event processing is simplified so less data has to be telemetered. MOS1 and MOS2 are orthogonal, so two projections at right angles are available if both cameras are in timing mode. This mode gives a timing resolution of 1.75 ms per row or time slice. An experimental full width timing mode can also be implemented to give around 10 ms resolution.

The choice of mode is based on the extent of the source and its brightness; for the majority of sources the basic mode is acceptable, and window or timing modes are selected to deal with pile-up in bright sources (Ballet, 1999). For source strengths below a few counts per second, the flux within the PSF is small enough that the probability of interference between the pixel patterns of individual photons is small. In this case there is no error in either flux or photon energy determination, and pile-up is negligible. As the flux increases the patterns from successive photons detected in the 2.6 s integration time start to interfere, and pile-up becomes significant. In the MOS cameras the dominant effect of pile up is a loss of flux; there is little distortion of the energy spectrum. This is because early pile-up results in the generation of non-X-ray-like event patterns, caused by contact between two genuine patterns; such events are removed automatically from the data stream by the EMCR, and do not appear in the spectrum. The PSF has a very sharp core, and this means that the flux-loss associated with pile-up occurs first in the core of the PSF, while the wings remain unaffected: a typical indicator of pile-up is a source cross section in the image with a depressed central region. Since flux removal is the main effect it is moderately safe to form the spectrum from the remaining flux even though the centre of the PSF is missing. In general it is safe to err towards imaging mode or large windows, unless the source is very bright.

Timing is related to the CCD readout and through the electronics to the spacecraft clock. The precision of timing is limited to the effective integration time. The accuracy is achieved via the spacecraft clock to UTC, and for a given sample there is a ±40 μs jitter caused by the fine time code sampling of this clock.

6. The EPIC MOS Response Function

The CCDs image the entire field of view and give an energy value and position to all X-ray photons detected. The flux and spectrum of X-ray sources in the field of view can be determined from the charge measured in the individual photon event by the EMCR, the redistribution matrix of the CCD, and its quantum efficiency. These have been determined by a combination of ground calibration using the Orsay synchrotron (Pigot et al., 1999; Trifoglio et al., 1998), and celestial source calibration since launch. The current relative accuracy of calibration is better than 10% over the energy range from 0.2 to 10 keV. X-ray photons falling on the CCD can be absorbed in the electrode structure, in the depleted silicon, or in the field-free un-depleted silicon. A photon absorbed in the electrode structure is lost; one converting in the depleted region is detected with all its energy; one converting in the field free region is detected, but some energy may be lost. These factors go together to make up the quantum efficiency of the device. In the case of the CCD22 the open phase produces additional complication because the low energy photons detected can interact either in the pinning implant, or in the depleted silicon beneath it. In the implant region a certain fixed amount of charge can be lost. So for soft photons there may be a low energy 'shoulder' on the peak observed for a monochromatic X- ray beam, or even a double peak; this degrades the energy resolution. These surface loss events have been carefully calibrated using data from monochromatic X-ray beams in the Orsay synchrotron (Pigot et al., 1999; Dhez et al., 1997), and celestial sources; some examples are shown in figure 5 for different energies. This effect is fully taken into account in the calibration files. The quantum efficiency of the CCDs is a smooth function except near the edges of silicon and oxygen; the carbon and aluminium edges are apparent in the thin and medium filter responses, tin appears as well in the thick filter (the gold edges of the mirror are apparent in the overall quantum efficiency). The response near these edges was measured using different beams at the Orsay synchrotron. The measurements have been linked together using celestial sources, especially BL Lac objects that have a smooth featureless spectrum, and the Crab nebula spectrum, which is likewise featureless. The current quantum efficiency curve is shown in figure 6. It varies a little from CCD to CCD at very low energies. The energy assigned to a photon is calculated from the charge in the pixel pattern. Most of the photons

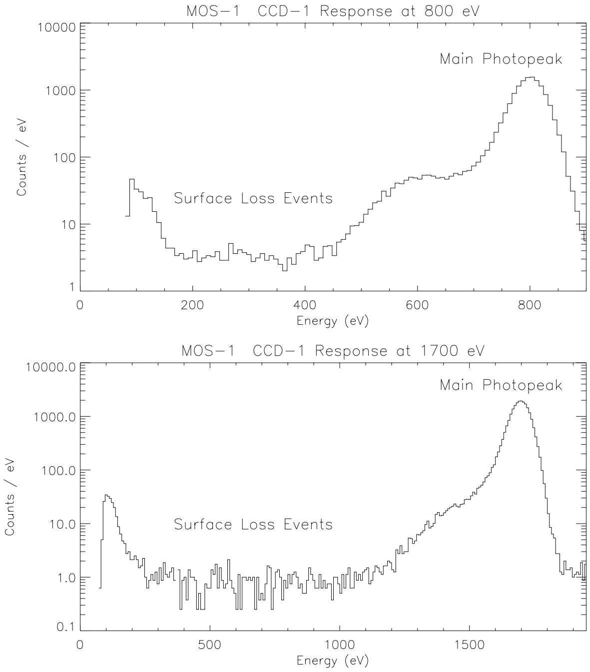

Fig. 5. The energy redistribution function of the MOS CCDs for monochromatic X-rays of different energies, as measured at the Orsay synchrotron

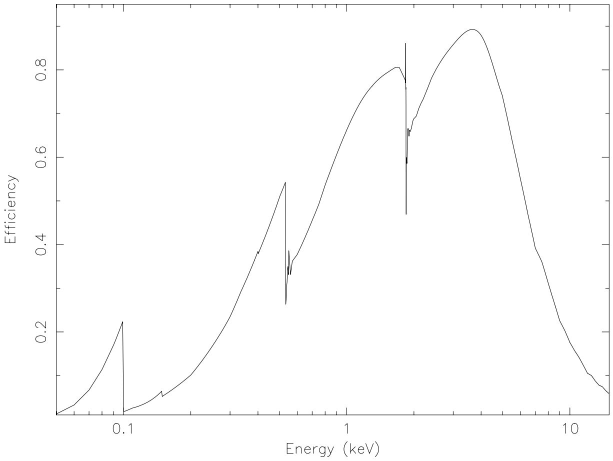

Fig. 6. The X-ray quantum efficiency of the EPIC MOS CCDs based on the Orsay synchrotron measurements and celestial source measurements

detected in EPIC MOS give single pixel events. For two, three, and four pixel events, the charge is summed over the relevant pixels. The event patterns recognised by the EMCR are shown in figure 7. Patterns zero to twelve are X-ray events while the rest are not, with the exception of pattern 31. This is formed by cosmic rays and also by deeply interacting energetic X-rays. All of these effects are included in the published calibrations of the EPIC MOS; we are working to improve calibration, and this will be reflected in subsequent issues.

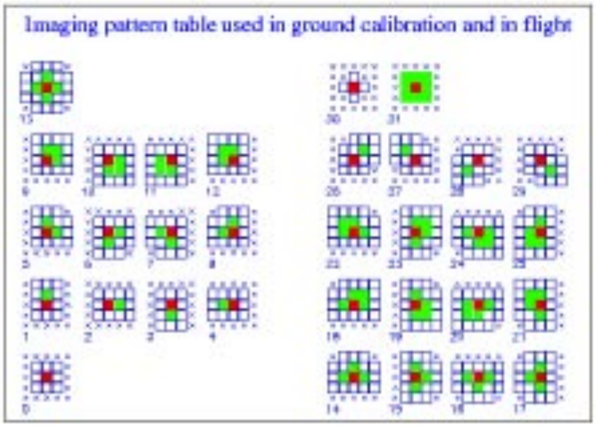

Fig. 7. The event patterns recognised by the EMCR in the imaging modes. The coding is the following : the red pixel is the centre pixel, its signal is above threshold and is the largest signal in the 3 × 3 inner matrix; the green pixels have signals above threshold; the white pixels have signal below threshold; the crosses indicate pixels not considered.

7. The Filters

The EPIC cameras are provided with light and UV blocking filters. There are four filters in each camera (Villa et al., 1997; Stephan et al., 1996). Two are thin filters made of 1600 Å of poly-imide film with 400 Å of aluminium evaporated on to one side; one is the medium filter made of the same material but with 800 Å of aluminium deposited on it; and one is the thick filter. This is made of 3300 Å thick Polypropylene with 1100 Å of aluminium and 450 Å of tin evaporated on the film. Poly-imide is opaque to UV, but polypropylene is not, hence the tin. The filters are self-supporting and 76 mm in diameter. The remaining two positions on the filter wheel are occupied by the closed and open positions respectively. The closed position has 1.05 mm of aluminium, and the open position has nothing. The former is used to protect the CCDs from soft protons in orbit, while the open position can be used for observations where the light flux is very low, and no filter is needed. Light falling on the CCDs increases the baseline charge level in the exposed pixels; this adds on to charge measured when an X-ray photon falls on an affected pixel. It only has an effect where X-ray photons fall, e.g. a bright optical point source in an image will have no effect on X-ray sources unless it coincides or overlaps with one of them; scattering and the wings of the PSF have to be taken into account in defining overlap. Diffuse illumination will have an effect over the whole focal plane. In general diffuse optical illumination is very low in EPIC, so the filter should be selected for the optical flux of the source being observed. The the X-ray transmission as a function of photon energy are shown in figure 8.

8. On-Board Calibration Source

A calibration source is fitted to each camera to allow the absolute energy to be calculated to an accuracy of a few eV; this is

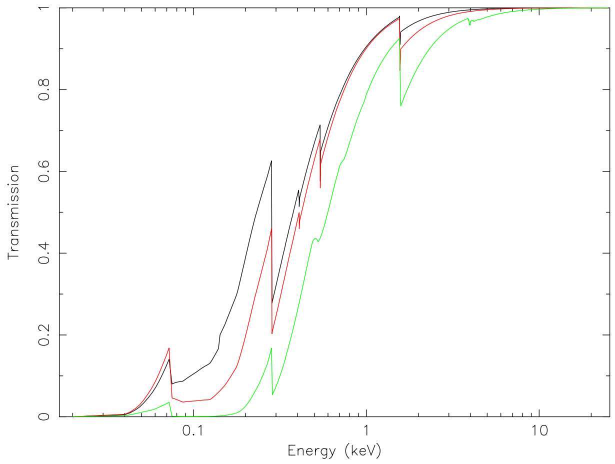

Fig. 8. The X-ray transmission of the thin(black), medium(red) and thick(green) filter

important for line velocity measurements. The source uses iron 55, and provides Al K_α, Mn K_α and Mn K_β and lines at 1.5, 5.9 and 6.5 keV respectively. It can illuminate the whole focal plane, for any filter position, by means of small slots in the filter wheel that can be brought into effect by a small additional rotation once the filter is positioned. This enables the gain of the system to be measured for the same conditions and time as the observation. It should be noted that for all CCDs there is a dependence of measured charge on the position where the photon was detected within the CCD. This is caused by charge loss during transfer of the photon event from its detected position to the readout node. This is expressed by the Charge Transfer Efficiency of the CCD. The monochromatic synchrotron data was used to determine and correct the average charge transfer losses for the MOS CCD readout, prior to generating the response function. The CTE is degraded by radiation damage in-orbit, and already this can be detected after nine months in orbit, see figure 9. However, this degradation, if left uncorrected, would represent a loss of spectral resolution of less than 2%. The spatial correction employed will be progressively updated during the life of the EPIC MOS cameras. The correction can be established using the on-board calibration source.

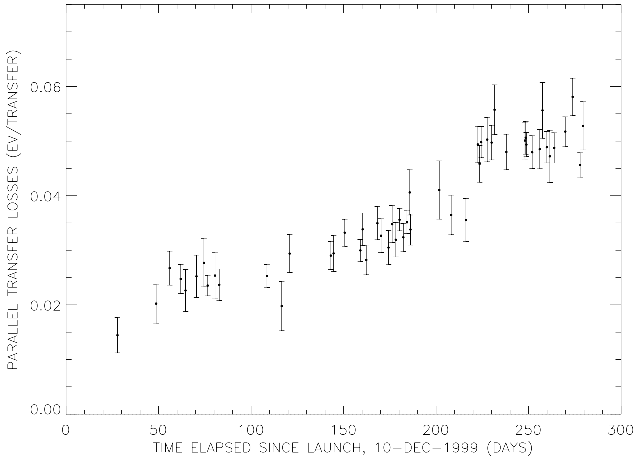

Fig. 9. The evolution of spatial charge loss with time since launch in eV channels per pixel as measured in the Mn K_α line. A step at day $\sim$ 220 can be seen corresponding to a very large solar flare.

9. Radiation Damage and Precautions

EPIC CCDs (MOS & PN), have a high degree of immunity to ionisation damage, they are however sensitive to displacement-damage by protons with energy between 150 keV and 10 MeV: atoms in the silicon lattice are displaced, creating a damage site of locally low potential wherein charge can be trapped. Damage sites in the buried channel, through which the X-ray generated charge is transferred to the read-out node, hold back some electrons; delayed electrons are not included when the charge due to the X-ray event is determined. They are released later by thermal motion, the trapping time depending inversely on the temperature of the CCD. By increasing the density of charge passing through the buried channel, the loss can be reduced for normal operating temperatures; this occurs because a leading electron fills the trap, which then remains inactive, until the electron is released. The other electrons pass the inactive trap safely. By confining the electrons to a narrow buried channel during transfer, fewer traps are encountered and the charge-loss is further reduced. This is the reason for the current high CTE of the MOS CCDs (Holland et al., 1990). If the CCD is operated at a very low temperature (Holland, 1992) then the trapping time becomes very long, and the trap is essentially masked permanently. The MOS cameras have reserve cooling power to allow operation at 140 K. This precaution is not yet necessary, but will, when damage becomes severe, recover most of the consequent CTE loss as shown in figure 10. Presently the CCDs are operated at 170 K, to minimise condensation build-up on the CCDs. Because the most damaging protons are non-relativistic (they have a high displacement cross-section), the 3 cm shielding is effective (below 30 MeV). More energetic protons can penetrate the shielding, but their flux and cross section are much lower. In combination with the extra cooling this shielding was expected to be sufficient to protect the CCDs over the ten-year lifetime of XMM-Newton, taking into account the orbital evolution. It is now known that very soft protons can be focused by the X-ray mirrors, and reach the CCDs, by-passing the shielding (Rasmussen et al., 1999). These protons stop in less than a micron of material; in MOS CCDs the buried channel lies only 0.5 microns below the surface, so they can cause very significant damage; two orders of magnitude greater than 10 MeV protons. The large effective area of the XMM-Newton mirrors makes this focused soft proton flux very high, and the potential for damage very serious. Fortunately the closed position of the filter wheel places 1.05 mm of aluminium in the focused beam and completely stops the protons. For all perigee passages the filter wheel is rotated to the closed position before the spacecraft encounters the outer radiation belts. This has prevented damage by soft protons in the belts. Soft protons are also found outside the belts, prob-

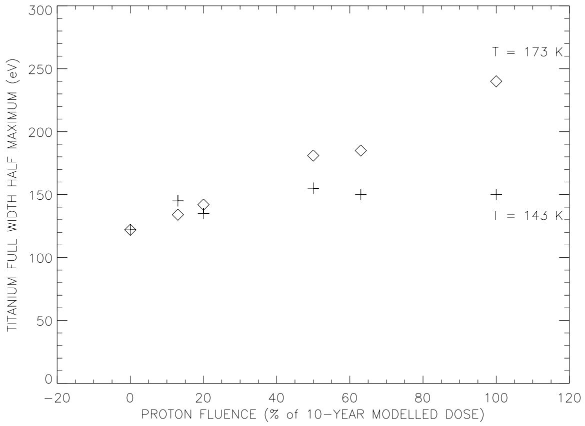

Fig. 10. The recovery of radiation damage on CCD 22 with cooling. The damage was induced by 10 MeV protons at the Birmingham University Cyclotron. The full scale is approximately equivalent to ten years operation in orbit, based on pre-launch calculations.

ably accelerated in the magnetopause. When the flux of these is high the filter wheel is rotated to the closed position to protect the CCDs. Lower fluxes can contribute to the background in the image during observations. They stop close to the surface of the silicon and generate single pixel events with a flat energy spectrum; they are indistiguishable from X-rays. It is not known if the prevalence of these clouds of soft protons will change as solar activity decreases, or as the orbit of XMM-Newton evolves. On average several hours per orbit have a high soft proton background, or are lost completely because the filter wheel has to be closed. Figure 11 shows an image collected while the soft proton flux was relatively high compared with a low proton flux image. There have been two large solar flares so far since the launch of XMM-Newton. These generate high fluxes of penetrating protons that cause CCD damage through the shielding; they are not focused by the mirrors. After the first flare a measurable degradation of the CTE was observed, equivalent to several months' passages through the radiation belts. Thus the CTE falls steadily due to the latter effect while solar flares generate steps in the curve, as shown in figure 9. If the CTE is degraded seriously, and extra cooling cannot recover it, annealing of the CCDs can be attempted by heating the CCD mounting plate to 130°C. This should remove the damage, but carries a risk to the CCDs and their connections. It will only be used as a last resort.

9.1. Contamination

When there is a direct path from the interior of the optical bench to the cold surface of the CCD, it is possible for ice to build up on the CCD caused by water outgassed by the spacecraft. The filter, which is at about -20°C, provides a warm primary barrier to molecules, but the gaps around the filter can allow molecules to reach the CCD surface by several bounces. So far there is no evidence of ice build-up. If this is detected later on, then the filter wheel can be put in the open position and the CCDs heated to drive off the ice.

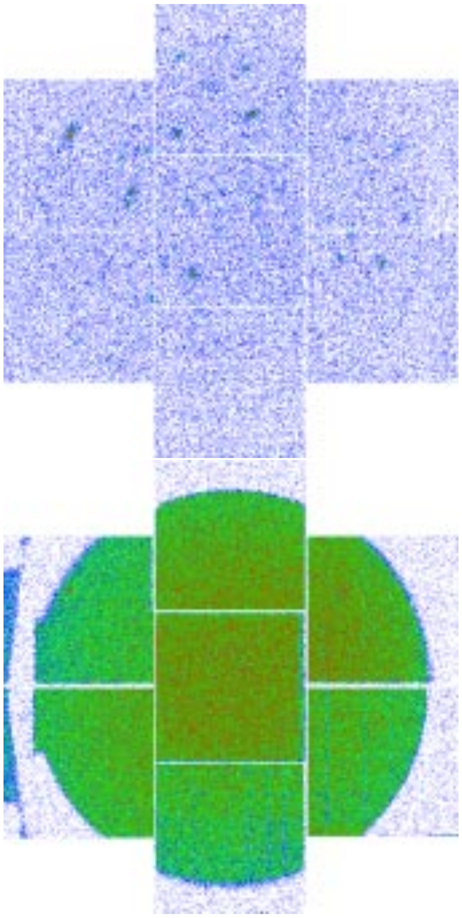

Fig. 11. Two images made with different soft proton backgrounds. The brightness of the background where the flux is high (bottom) is sharply shadowed by the metalwork of the camera. In the low flux image (top) the background is not enough to delineate the metalwork.

10. Background

The dark current and effects of light will be negligible in most circumstances for EPIC opbservations. Cosmic rays are removed on-board by the EMCR. The background in the image therefore consists of X-ray like events, and some electronic pattern noise. The latter appeared in orbit, not having been seen during ground testing, and results in a grid pattern appearing on images integrated for a long time. It is probably generated by low level EMC but the mechanism remains obscure. Fortunately only a few pixels are affected per frame, and these can easily be removed from the image by a simple algorithm, with negligible loss of X-rays. The remaining background is X-ray like and cannot be removed. It is made up of the small residuum from the removal of cosmic rays, the diffuse X-ray background, Compton interactions of cosmic and locally generated gamma rays, and soft protons. The soft protons can be removed or minimised by excluding periods when they are present; this is indicated by flaring in the count-rate from the outer CCDs. Nonflaring periods may represent an absence of soft protons or simply a low and steady flux of them. The gamma ray and cosmic ray induced background cannot be removed. The flux appears to be twice as big as predicted for this orbit; this may be related to the active state of the sun, or to inadequacies in the radiation models. The spectra of the soft proton and gamma induced backgrounds are much flatter than those of the diffuse X- ray background and of X-ray sources. So the effect on sensitivity is more marked at the higher energies. The cameras were designed to minimise the number of different materials that can generate fluorescent X-ray lines. Only silicon and aluminium lines appear in the background, at fairly low levels.

Acknowledgements. Based on observations obtained with XMM-Newton, an ESA science mission with instruments and contributions directly funded by ESA Member States and the USA (NASA). EPIC was developed by the EPIC Consortium led by the Principal Investigator, Dr. M. J. L. Turner. The consortium comprises the following Institutes: University of Leicester, University of Birmingham, (UK); CEA/Saclay, IAS Orsay, CESR Toulouse, (France); IAAP Tuebingen, MPE Garching,(Germany); IFC Milan, ITESRE Bologna, OAPA Palermo, Italy. EPIC is funded by: PPARC, CEA, CNES, DLR and ASI. The EPIC collaboration wishes to thank EEV Ltd, now Marconi Advanced Technology, MMS Stevenage and LABEN S.p.A-Milano for their dedication to the EPIC program.

References

Aschenbach, B. et al., 2001, A&A this volume

Ballet, J., 1999, A&AS 135, 371

Boër, M., Naya, J., Chabaud, J. P., Ehanno, M., Rouaix, G., Baiget, A., Ecoffer, R., Labrunne, M., Calvel, P., and Reveret, P., 1996, IEEE Trans. Nucl. Sci.

Brinkman, A. C. et al., 2001, A&A this volume

Butler, I. G. and Goodall, C. V., 2000, J. of Aero. Eng. p. submitted

Dhez, P., Jourdain, E., Hainaut, O., Hochedez, J. E., Labeque, A., Salvetat, P., and Song, X. Y., 1997, Proc. SPIE 3114, 134

Ferrando, P., Arnaud, M., Bouére, A., Cara, C., Lortholary, M., Pigot, C., Sauvageot, J. L., and Schmitt, D., 1999, Astron. Nachr. 320 (4/5), 379

Holland, A., Abbey, A., Lumb, D., and McCarthy, K., 1990, Proc. SPIE 1344, 378

Holland, A. D., 1992, NIM A326, 335

Jansen, F. et al., 2001, A&A this volume

Pigot, C., Belsole, E., Bennie, P. J., Ferrando, P., Sauvageot, J. L., Marty, P. B., and Sembay, S., 1999, Proc. SPIE 3765, 251

Pigot, C., Sauvageot, J. L., Ferrando, P., and Belsole, E., 2000, Proc. SPIE 4140

Rasmussen, A., Chervinsky, J., and Golovchenko, J., 1999, RGS-COL-CAL-99009

Short, A. D., Keay, A., and Turner, M. J., 1998, Proc. SPIE 3445, 13

Stephan, K., Reppin, C., Hirschinger, M., Maier, H. J., Frischke, D., Fuchs, D., Mueller, P., and Guertler, P., 1996, Proc. SPIE 2808, 421

Strüder, L. et al., 2001, A&A this volume

Trifoglio, M., Gianotti, F., Stephen, J. B., Balasini, M., Hochedez, J. E., Chiappetti, L., Glukhov, R. A., Hainaut, O., Jourdain, E., La Palombara, N., Marty, P. B., Moreno, T., and Musso, C., 1998, Proc. SPIE 3445, 558

Villa, G. E., Abbey, A. F., Arnaud, M., Balasini, M., Bignami, G. F., Boer, M., Brauninger, H., Butler, I., Cafagna, G., Cara, C., Chabaud, C., Chiappetti, L., Cole, R. E., Conte, M., Dowson, J., Dhez, P., Duc, R., di Cocco, G., Ferrando, P., Goodall, C. V., Hippman, H., Holland, A. D., Kendziorra, E., Labeque, A., Meidinger, N., Moriggio, C., La Palombara, N., Musso, C., Poindron, E., Peres, G., Pferrerman, E., Pigot, C., Pye, J. P., Reppin, C., Schmitt, D., Sciortino, S., Serio, S., Spragg, J., Stephen, J. B., Struder, L., Trifoglio, M., Tua, P., Turner, M. J., and Whitehead, S., 1996, Proc. SPIE 2808, 402

Villa, G. E. et al., 1997, IEEE Transactions in Nuclear Science

Willingale, R., Aschenbach, B., Bonnet-Bidaud, J. M., Griffiths, R. G., Sembay, S., Warwick, R. S., and Becker, W., 2001, A&A this volume